ROYAL SOCIETY
OF CHEMISTRY

PAPER

Upper limit to the photovoltaic efficiency of imperfect crystals from first principles†

Sunghyun Kim, [iD] [a] José A. Márquez, [iD] [b] Thomas Unold [iD] [b] and Aron Walsh [iD] *[ac]

The Shockley–Queisser (SQ) limit provides a convenient metric for predicting light-to-electricity conversion efficiency of a solar cell based on the band gap of the light-absorbing layer. In reality, few materials approach this radiative limit. We develop a formalism and computational method to predict the maximum photovoltaic efficiency of imperfect crystals from first principles. The trap-limited conversion efficiency includes equilibrium populations of native defects, their carrier-capture coefficients, and the associated recombination rates. When applied to kesterite solar cells, we reveal an intrinsic limit of 20% for $Cu_2ZnSnSe_4$, which falls far below the SQ limit of 32%. The effects of atomic substitution and extrinsic doping are studied, leading to pathways for an enhanced efficiency of 31%. This approach can be applied to support targeted-materials selection for future solar-energy technologies.

Sunlight is the most abundant source of sustainable energy. Similar to the Carnot efficiency of heat engines, the maximum efficiency for photovoltaic energy conversion is determined by thermodynamics and can be as high as 86% owing to the high temperature of the sun.[1,2] However, in practical solar cells with single p–n semiconductor junctions, large irreversible energy loss occurs mainly through hot-carrier cooling and low light absorption below the band gap.[3]

The Shockley–Queisser (SQ) limit describes the theoretical sunlight-to-electricity conversion efficiency of a single-junction solar cell.[3] The SQ limit (33.7% under AM1.5g illumination) and its variations, including spectroscopic limited maximum efficiency (SLME),[4] determine the maximum efficiency of a solar cell based on the principle of detailed balance between the absorption and emission of light. The amount of photons absorbed determines the short-circuit current density J_{SC}, and, hot-carrier cooling and radiative recombination limit the maximum carrier concentration and hence the open-circuit voltage V_{OC}.

In the SQ limit, the predicted efficiency is a function of the semiconductor band gap, which is a trade-off between light absorption (current generation) and energy loss due to hot-carrier cooling. This analysis secured the band gap as a primary descriptor when searching for new photovoltaic compounds,

often within a 1–1.5 eV target window. Unfortunately, few materials approach the SQ limit. Less than 10 classes of materials have achieved conversion efficiency greater than 20%.[5] Most emerging technologies struggle to break the 10% efficiency threshold.

Kesterites are a class of quaternary materials studied for thin-film photovoltaic applications. Although a lot of progress has been made during the past few decades, the certified champion efficiency of 12.6%[6] has been increased by less than 0.1% since 2013.[7] The main bottleneck is the low open-circuit voltage, which is far below the SQ limit.[8] Many routes to engineer compositions and architectures have been considered, but it is not clear which process dominates.[9] One of the biggest questions in the field is if there is an intrinsic problem with kesterite semiconductors that prevent them approaching the radiative limit.[10–12]

The discrepancy between the SQ limit and efficiencies of real solar cells results from the extra irreversible processes such as electron–hole nonradiative recombination. While Shockley and Queisser studied the effect of the nonradiative recombination, it has been treated as a parameter of radiative efficiency and often a radiative efficiency of 100% is assumed, which is unrealistic for real materials.

The rate of nonradiative recombination mediated by traps can be described by Shockley–Read–Hall statistics.[13,14] The steady-state recombination rate is determined by the detailed balance where the net electron-capture rate is equal to the net hole capture rate. A microscopic theory of carrier capture was proposed by Henry and Lang in 1977.[15] The thermal vibration of the defect, together with the electron–phonon coupling, causes charge transfer from a delocalised free carrier to a localised defect state. Thus the carrier capture coefficient heavily depends on the electron and phonon wave functions

[a] Department of Materials, Imperial College London, Exhibition Road, London SW7 2AZ, UK. E-mail: a.walsh@imperial.ac.uk

[b] Helmholtz-Zentrum Berlin für Materialien und Energie GmbH, Department Structure and Dynamics of Energy Materials, Hahn-Meitner-Platz 1, D-14109 Berlin, Germany

[c] Department of Materials Science and Engineering, Yonsei University, Seoul 03722, Korea

This journal is © The Royal Society of Chemistry 2020

Energy Environ. Sci., 2020, **13**, 1481–1491 | **1481**

associated with a defect, which are difficult to probe experimentally. Instead, the microscopic processes in materials, including nonradiative carrier capture, have been inferred from macroscopic responses such as a capacitance transient.[15] Macroscopic properties of solar cells (*e.g.* open-circuit voltage and device efficiency) and microscopic processes in the material (*e.g.* carrier capture coefficient) are rarely connected. Therefore, although theories of solar cells are well known, the theoretical approaches have failed to provide *a priori* predictions of photovoltaic efficiencies of real materials.

Each material has a fundamental limit of radiative efficiency because the material contains a certain amount of native defects. Their concentrations in thermal equilibrium are intrinsic properties of the materials, and the resulting 'soup' of defects determines the maximum radiative efficiency. Recently, first-principles methods based on density functional theory (DFT) have been developed to calculate the nonradiative carrier capture,[16–18] which opens up the possibility for studying the theoretical upper-bound of photovolataic efficiency of a real material limited by both the radiative and the nonradiative recombination.

In this work, we propose a first-principles method of the trap-limited conversion efficiency (TLC) to calculate the upper-limit of photovolotaic efficiency of a material containing the number of native defects in thermal equilibrium. To take into account both radiative and nonradiative processes, we perform a series of calculations for kesterites. The absorption and the emission of light are calculated in the framework of Shockley and Queisser. To obtain the nonradiative recombination rate, we calculate the carrier capture coefficients and equilibrium concentrations of native defects. The workflow for our method is shown in Fig. 1. We conclude that kesterite solar cells suffer from significant nonradiative recombination and are unable to reach the SQ limit even under optimal growth conditions. Strategies to overcome such rapid recombination rates are suggested.

I. Theory

A. Radiative recombination

The short-circuit current J_{SC} of a solar cell whose absorber thickness is W is given by the absorbed photon flux multiplied by an elementary charge q:

$$J_{SC}(W) = q \int_0^\infty a(E; W) \Phi_{sun}(E) dE, \tag{1}$$

where $\Phi_{sun}(E)$ and $a(E;W)$ are the solar spectrum and the absorptivity at a photon energy E, respectively. Following the SQ limit, we assume that an absorbed photon generates one electron–hole pair.

The radiative recombination rate for the solar cell at temperature T is given by

$$\begin{aligned}
R_{rad}(V) &= \frac{2\pi}{c^2 h^3} \int_0^\infty a(E; W) \left[e^{E-qV/k_B T} - 1 \right]^{-1} E^2 dE \\
&\approx \frac{2\pi}{c^2 h^3} e^{\frac{qV}{k_B T}} \int_0^\infty a(E; W) \left[e^{E/k_B T} - 1 \right]^{-1} E^2 dE \\
&= R_{rad}(0) e^{\frac{qV}{k_B T}},
\end{aligned} \tag{2}$$

where V is a bias voltage representing the chemical potential of the electron–hole pair. At the short-circuit condition, the solar cell and ambient are in equilibrium: the radiative recombination rate $R_{rad}(0)$ is equal to the absorption rate from the ambient irradiation. The net current density J^{rad} limited by the radiative recombination is given by

$$J(V; W) = J_{SC}(W) + J_0^{rad}(W) \left(1 - e^{\frac{qV}{k_B T}} \right), \tag{3}$$

where the saturation current $J_0^{rad} = qR_{rad}(0)$.

In the SQ limit, an absorptivity is assumed to be a step function being 1 above the band gap E_g and 0 otherwise, while a
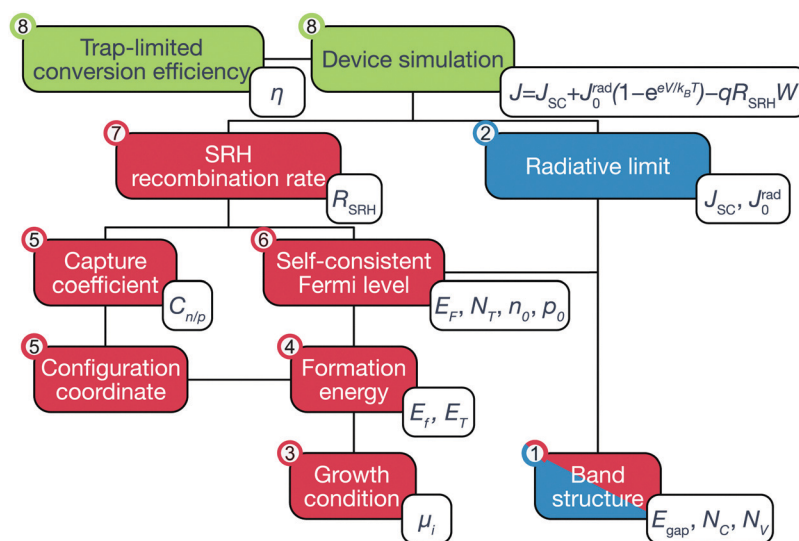

Fig. 1 Diagram for the calculation of trap-limited conversion efficiency. The dependent calculations are connected by lines. For each numbered step, the calculated quantities are appended. The red and blue boxes represent calculations for radiative and nonradiative electron–hole recombination, respectively. The combined device simulations are marked in green. The corresponding physical processes are detailed and illustrated in the ESI.†

real material has a finite absorptivity with a tail near the band gap E_g, which depends on the sample thickness. Rau et al.[19] defined a photovoltaic band gap using the absorption edge spectrum and found that, in inorganic solar cells, the effect of the finite absorption tail on the open-circuit voltage loss is small.[19]

B. Nonradiative recombination

A material in thermal equilibrium will contain a population of native defects. Defect processes are unavoidable and define the upper limit of performance of optoelectronic devices. The nonradiative recombination at charge carriers via defects is often a dominant source of degradation of solar cells and should be carefully controlled.[20]

Based on the principle of detailed balance,[13,14] the steady-state recombination rate R_{SRH} via a defect with electron-capture coefficient C_n and hole-capture cross coefficient C_p is given by

$$R_{SRH} = \frac{np - n_i^2}{\tau_p(n + n_t) + \tau_n(p + p_t)}, \quad (4)$$

where

$$\begin{aligned} \tau_n^{-1} &= N_T C_n = N_T \sigma_n v_{th,n}, \\ \tau_p^{-1} &= N_T C_p = N_T \sigma_p v_{th,p}. \end{aligned} \quad (5)$$

Here, n, p, and N_T denote concentrations of electrons, holes, and defects, respectively. n_i is an intrinsic carrier concentration ($n_i^2 = n_0 p_0$, where n_0 and p_0 are intrinsic electron and hole concentrations). n_t and p_t represent the densities of electrons and holes, respectively, when the Fermi level is located at the trap level E_T. The capture cross section (σ_n for electron and σ_p for hole) is commonly used in experimental studies, and can be calculated taking the thermal velocities of electron $v_{th,n}$ and hole $v_{th,p}$ to be 10^7 cm s^{-1}.

For doped semiconductors, minority carrier lifetime often determines the rate of the total recombination process. For example, in a p-type semiconductor where the acceptor concentration, p_0, is much higher than the photoexcited carrier density, the R_{SRH} due to a deep defect is proportional to the (photoexcited) excess carrier density Δn:[21]

$$R_{SRH} \approx \frac{\Delta n}{\tau_n} = \Delta n N_T C_n. \quad (6)$$

In case of a material containing many types of recombination centers, the total recombination rate R_{SRH} is the sum over all independent centers.

The calculation of R_{SRH} requires three properties of a defect (concentration N_T, defect level E_T, and capture coefficient $C_{n/p}$) in addition to the carrier concentrations n and p, as well as the intrinsic doping density n_0 or p_0 in the bulk host, as explained in the following subsections.

Equilibrium defect concentrations

Phase diagram. The growth environment of a crystal including elemental ratio, partial pressures, and temperature determines the properties of the material including concentrations of the native defects. In a theoretical framework, the growth conditions

can be expressed using the thermodynamic chemical potential μ of each element. We compare the energies of kesterites and their competing secondary phases, showing a range of chemical potentials that favors the formation of kesterites, using CPLAP.[27] We can avoid the formation of the secondary phases by a careful choice of synthesis conditions. However even 'pure' kesterites without secondary phases will contain native defects whose concentrations are controlled by this choice of chemical potentials.

Formation energy of a defect. We calculated the formation energy $\Delta E_f(D^q)$ of a defect D with the charge state q as given by[28]

$$\Delta E_f(D^q) = E_{tot}(D^q) - E_{tot}(\text{bulk}) - \sum_i N_i \mu_i + qE_F + E_{corr}, \quad (7)$$

where $E_{tot}(\text{bulk})$ and $E_{tot}(D^q)$ are the total energies of a bulk super-cell and a supercell containing the defect D^q, respectively. In the third term on the right-hand side, N_i is the number of atoms i added to the supercell, and μ_i is its chemical potential which is limited by the aforementioned phase diagram. E_F is the Fermi level, and E_{corr} is a correction term to account for the spurious electrostatic interaction due to periodic boundary conditions.[29,30]

Self-consistent Fermi level. For a given synthesis condition (set of atomic chemical potentials), the formation energy is a function of the Fermi level as shown in eqn (7), while the Fermi level is determined by the concentrations of charged defects and carriers. Thus we calculate the equilibrium concentrations of defects and carriers, and the Fermi level self-consistently under the constraint of charge neutrality condition for overall system of defects and charge carriers using SC-FERMI.[31]

For a given Fermi level, the equilibrium concentration of a defect $N(D^q)$ is given by

$$N(D^q) = N_{site} g e^{-\Delta E_f(D^q)/k_B T}, \quad (8)$$

where N_{site} and g are the number of available sites per unit volume and the degeneracy of the defect, respectively. In the dilute limit, the competition between defects is negligible. The partition function is approximated as 1 (i.e. the majority of lattice sites are regular). Note that we use the internal energy of formation to calculate the defect density, neglecting the vibrational entropy change. Thus the estimated defect densities are lower bounds.[32]

The concentrations of holes p_0 and electrons n_0 are determined by the effective density of states of valence band N_V and conduction band N_C:

$$\begin{aligned} p_0 &= N_V e^{-E_F - E_{VBM}/k_B T}, \\ n_0 &= N_C e^{-E_{CBM} - E_F/k_B T}. \end{aligned} \quad (9)$$

Here, E_{VBM} and E_{CBM} are the reference energies of the valence band maximum and conduction band minimum, respectively.

The net charge of defects should be compensated by the net charge of electrons and holes:

$$\sum_{i,j} q_j N(D_i^{q_j}) = p_0 - n_0. \quad (10)$$

This journal is © The Royal Society of Chemistry 2020

Energy Environ. Sci., 2020, **13**, 1481–1491 | **1483**

Thus, we iteratively update the Fermi level until the charge neutrality condition (eqn (10)) is satisfied. First, we determined the equilibrium concentration of defects at high temperature (T_{an} = 800 K) and equilibrated their charge states at room temperature (T_{op} = 300 K) with a fixed concentration of defects.

Defect levels. A defect can change its charge state by capturing or emitting carriers. The recombination process requires that defects are electrically active with more than one charge state. The energy required to change the charge state of the defect level is often referred to as a thermal activation energy or a charge-transition-level. In modern defect theory, the defect level D is calculated as the position of Fermi level where the formation energies with two charge states of q_1 and q_2 are equal:

$$E_T(q_1/q_2; D) = \frac{\Delta E_f(E_F = 0; D^{q_1}) - \Delta E_f(E_F = 0; D^{q_2})}{q_2 - q_1}. \quad (11)$$

Carrier capture coefficient. Nonradiative carrier capture via a defect is triggered by a vibration and the associated electron–phonon coupling between the localised trap state and the delocalised free carriers. The initial excited state, for example, a positively charged donor (D^+) with an electron in the conduction band (e^-), vibrates around the equilibrium geometry. The deformation of the structure causes the electronic energy level of the trap state to oscillate. As the energy level approaches the conduction band, the probability for the defect to capture the electron increases significantly. When the electron is captured, the donor becomes neutral D^0 and relaxes to a new equilibrium geometry by emitting multiple phonons. To describe and predict such a process, quantitative accounts of the electronic and atomic structures, as well as vibrational properties of the defect are essential.

The carrier capture coefficient C can be expressed using the electron–phonon coupling W_{ct} and the overlap of phonon wave functions $\langle \xi_{cm} | \Delta Q | \xi_{tn} \rangle$,[17,18] which is given by

$$C = \Omega g \frac{2\pi}{\hbar} |W_{ct}|^2 \sum_{m,n} w_m |\langle \xi_{tn} | \Delta Q | \xi_{cm} \rangle|^2 \quad (12)$$
$$\times \delta(\Delta E + \varepsilon_{cm} - \varepsilon_{tn})$$

where Ω and g denote the volume of supercell and the degeneracy of the defect, respectively. ξ represents the phonon wave function, and the subscripts c and t specify the free carrier and trap states, respectively. In this formalism, the temperature-dependence is determined by the thermal occupation number w_m of the initial vibrational state. In the following discussion, we calculate the capture coefficients at room temperature. We employ an effective configuration coordinate ΔQ for the phonon wave functions and adopt static coupling theory for W_{ct}. The Coulomb attraction and repulsion between charged defects and carriers are accounted for by the Sommerfeld factor.[33,34] See ESI† for details.

Steady-state illumination. Under illumination or bias voltage, the steady-state electron and hole concentrations deviate from those determined by the equilibrium Fermi level. The amount of applied voltage V is the difference between the electron and hole

quasi-Fermi levels ($E_{F,n}$ for electron and $E_{F,p}$ for hole) which are functions of an additional carrier concentration Δn:

$$\begin{aligned} qV(\Delta n) &= E_{F,n}(\Delta n) - E_{F,h}(\Delta n) \\ &= E_{CBM} + k_B T \ln\left(\frac{n_0 + \Delta n}{N_C}\right) \\ &\quad - E_{VBM} + k_B T \ln\left(\frac{p_0 + \Delta n}{N_V}\right) \\ &= E_g + k_B T \ln\left(\frac{(n_0 + \Delta n)(p_0 + \Delta n)}{N_C N_V}\right), \end{aligned} \quad (13)$$

where we ignore the voltage drop due to a series resistance and a shunt across the device. One can rewrite eqn (13) for Δn as a function of V:

$$\Delta n(V) = \frac{1}{2}\left[-n_0 - p_0 + \sqrt{(n_0 + p_0)^2 - 4n_i^2\left(1 - e^{\frac{qV}{k_B T}}\right)} \right], \quad (14)$$

where $n_i^2 = n_0 p_0 = N_C N_V e^{\frac{-E_g}{k_B T}}$. Accordingly, the steady-state concentrations of electron n and hole p under applied voltage V are given by

$$\begin{aligned} n(V) &= n_0 + \Delta n(V), \\ p(V) &= p_0 + \Delta n(V). \end{aligned} \quad (15)$$

C. Trap-limited conversion efficiency

By taking into account the carrier annihilation due to both radiative recombination (eqn (3)) and nonradiative recombination (eqn (4)), the trap-limited current density J under a bias voltage V is given by

$$\begin{aligned} J(V; W) &= J_{SC}(W) + J_0^{rad}(W)\left(1 - e^{\frac{qV}{k_B T}}\right) \\ &\quad - qR_{SRH}(V)W. \end{aligned} \quad (16)$$

The voltage-dependent nonradiative recombination rate R_{SRH} is obtained by combining eqn (4), (8), (11), (12), and (15). Finally, we evaluate the photovoltaic maximum efficiency:

$$\eta = \max_V \left(\frac{JV}{q \int_0^\infty E \Phi_{sun}(E) dE} \right). \quad (17)$$

II. Results

We apply our scheme to kesterite solar cells ($Cu_2ZnSnSe_4$, Cu_2ZnSnS_4, $Cu_2ZnGeSe_4$, and $Ag_2ZnSnSe_4$), with details presented in the Methods section and Tables S1 and S2 (ESI†).

A. $Cu_2ZnSnSe_4$ and Cu_2ZnSnS_4

Shockley–Queisser limit. In the SQ limit under 1 sun (AM1.5g) illumination, the maximum efficiency of CZTSe with a band gap of 1 eV is 31.6% (see Fig. 2) with a V_{OC} of 0.77 V. Next, we calculate the nonradiative recombination rate due to native defects.

Growth conditions. Single-phase CZTSe is formed when the chemical potential of the elements are in the phase field of
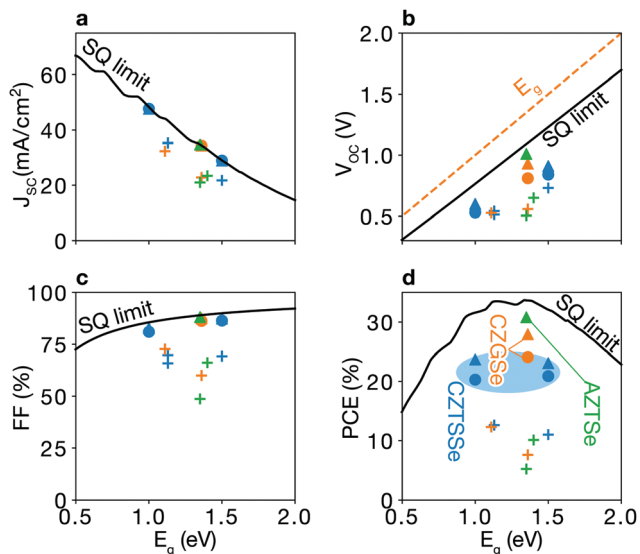
1484 | *Energy Environ. Sci.*, 2020, **13**, 1481–1491

This journal is © The Royal Society of Chemistry 2020

Fig. 2 Shockley–Queisser limit and trap-limited-conversion efficiency. (a) Short-circuit current density J_{SC}, (b) open-circuit voltage V_{OC}, (c) fill factor FF, and (d) efficiency η. Filled symbols represent the trap-limited conversion (TLC), while a black line is the SQ limit. TLCs with doping (triangles) show better performances as compared to TLCs without doping (circles). Plus signs indicate experimental data for kesterite solar cells taken from ref. 6, 7 and 22–26. The detailed values are listed in Table 1.

CZTSe as shown in Fig. 3a. The phase diagram of CZTSe has a small volume with a narrow window of available chemical potentials, which the stability of ZnSe is largely responsible for. At high Zn-ratio, Zn atoms tend to form ZnSe rather than to incorporate at their lattice sites in CZTSe. Later, we will show that this poor incorporation of Zn results in high concentrations of antisite defects: Cu_{Zn} and Sn_{Zn}, which are responsible to the p-type Fermi level and the low carrier lifetime, respectively.

Defect levels. Point defects introducing defect levels close to the band edge are categorized as shallow and generate free carriers.[20] On the other hand, deep defects are often responsible for carrier trapping and nonradiative recombination, limiting the efficiency of solar cells.[20]
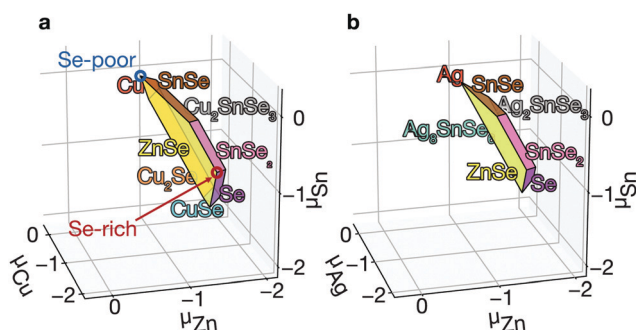

Fig. 3 Growth condition. Calculated phase diagrams of $Cu_2ZnSnSe_4$ (a) and $Ag_2ZnSnSe_4$ (b) where $\mu_i = 0$ represents the chemical potential of element i in its elemental state. Each plane represents a phase boundary with the secondary phase. Blue and red circles indicate Se-poor and Se-rich conditions, respectively.

The band structure of CZTSe is composed of antibonding Sn 5s–Se 4p* state at the lower conduction band and antibonding Cu 3d–Se 4p* state at the upper valence band. According to models for defect tolerance,[35,36] the Cu dangling bond would produce a shallow level, while a deep level can be introduced by the Sn dangling bond. Moreover, the cation antisites, especially $(Cu,Zn)_{Sn}$ and $Sn_{(Cu,Zn)}$ are expected to be deep due to the large difference in the site electrostatic (Madelung) potentials.[37]

Admittance spectroscopy (AS) measurements identified several shallow acceptors in Cu₂ZnSn(S,Se)4, CZTSSe, CZTSe and CZTS at an energy range between 0.05–0.17 eV,[38–43] which were attributed to V_{Cu} and Cu_{Zn}. They also found a deep level close to the midgap ($E_T = 0.5$ eV). A series of deep-level transient spectroscopy (DLTS) experiments also revealed the presence of the shallow levels as well as a broad spectrum of deep levels around the mid gap.[44–46] Transient photocapacitance (TPC) spectra showed sub-band-gap absorption via deep defects near 0.8 eV with broad bandwidth.[47,48] Theoretical calculations[37,49–51] revealed the atomic origins of shallow defects: acceptors V_{Cu} and Cu_{Zn} and a donor Zn_{Cu}. Several atomic models for the deep defects have been proposed such as $(Cu_3)_{Sn}$, Sn_{Zn}, V_S, $V_S–Cu_{Zn}$, and $Sn_{Zn}–Cu_{Zn}$.[37,49–51]

First, we find shallow acceptors (V_{Cu} and Cu_{Zn}) and a shallow donor (Zn_{Cu}) (see Fig. 4a and Table S3, ESI†). Due to the similar ionic radii of Cu and Zn, the energy cost for the formation of Cu_{Zn} and Zn_{Cu} is very low. The very low formation energy of Cu_{Zn} for every set of chemical potentials is largely responsible for the p-type Fermi level around 0.2 eV. We find that the decrease in oxidation state of Sn found in V_{Se}, Sn_{Zn} and $V_{Se}–Cu_{Zn}$ produces deep levels, similar to those found in CZTS.[37,49–51] The deep donor Sn_{Zn} becomes shallow when it combines with Cu_{Zn} because of the Coulomb attraction between the ionized donor and acceptor.[50]

Capture coefficients. As Cu-based kesterites are intrinsic p-type semiconductors, the carrier lifetime is determined by the electron-capture processes via deep defects. We calculate electron-capture coefficients of the selected deep defects: $V_{Se}–Cu_{Zn}$ and Sn_{Zn}, satisfying the criterion $E_{CBM} − E_T > E_{VBM} − E_F + 0.1$ eV so that $n_t \ll p$ at $T = 300$ K, and $N_T > 10^{14}$ cm^{-3}.

Due to the Sn reduction associated with these defects, they exhibit not only a deep level, but also a large structural relaxation that leads to large electron-capture coefficients.[37,50] Fig. 5a shows the configuration coordinate for $Sn_{Zn}(2+/1+)$, illustrating that the carrier-capture barrier is small due to the large lattice relaxation, the horizontal shift of the potential energy surface of Sn_{Zn}^{1+} with respect to that of Sn_{Zn}^{2+}. Thus, we find that $Sn_{Zn}(2+/1+)$ has a large electron-capture coefficient of 9×10^{-7} cm^3 s^{-1} (corresponding to the capture cross section of 9.29×10^{-14} cm^3 s^{-1}), which classify them as killer centers.[52] Note that the minority-carrier capture coefficient of these native defects in CZTSe are of a similar order of magnitude of the most detrimental extrinsic impurities in Si solar cells.[53,54] We also find a large electron-capture coefficient of $V_{Se}–Cu_{Zn}$, which is listed in Table S3 (ESI†).

Equilibrium concentration. The concentration of native point defects can be tuned through the chemical environment. However, we find that it is difficult to reduce the concentration of the killer centers in CZTSe. For example, to reduce the
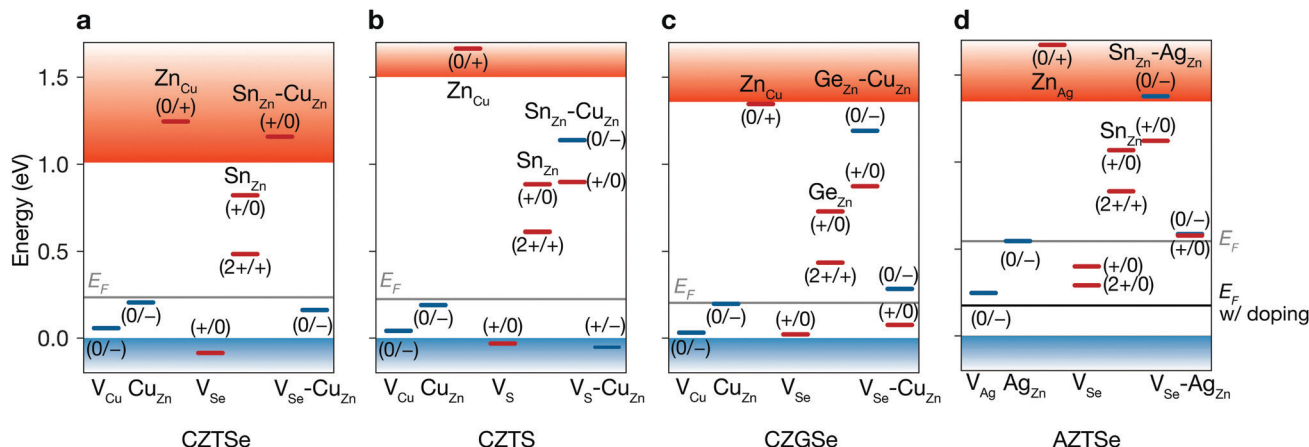
This journal is © The Royal Society of Chemistry 2020

Energy Environ. Sci., 2020, **13**, 1481–1491 | **1485**

Fig. 4 Defect levels of native defects. Donor (red) and acceptor (blue) levels of native point defects of $Cu_2ZnSnSe_4$ (a), Cu_2ZnSnS_4 (b), $Cu_2ZnGeSe_4$ (c), and $Ag_2ZnSnSe_4$ (d). Blue and red bands represents valence and conduction bands, respectively. Fermi levels are shown in gray lines. The black line in d represents the Fermi level of $Ag_2ZnSnSe_4$ with a doping density of 10^{20} cm^{-3}.
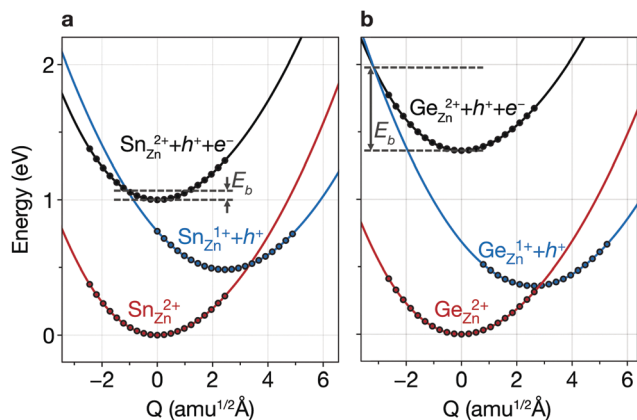

Fig. 5 Configuration coordinate diagram for carrier capture. Potential energy surfaces for the vibrations of Sn_{Zn} (2+/+) in $Cu_2ZnSnSe_4$ (a) and Ge_{Zn} (2+/+) in $Cu_2ZnGeSe_4$ (b). The solid circle represents the relative formation energy calculated using DFT, and the line is a spline fit. E_b represents the electron-capture barrier.
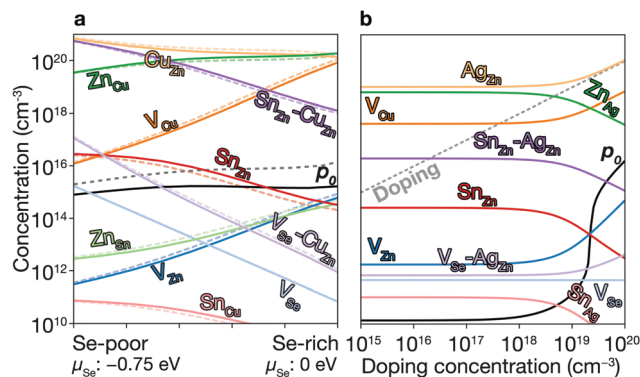

Fig. 6 Concentrations of native defects. (a) The concentrations of native defects in CZTSe. The dashed lines represent the concentration with the doping during the growth (see text for details). (b) The concentrations of native defects in AZTSe with the doping during the growth. The dashed diagonal line represents the doping concentration.

concentration of Sn_{Zn}, we need: (i) to increase Zn incorporation, (ii) to decrease Sn incorporation, or (iii) to decrease hole concentration. These are difficult to achieve due to the narrow thermal equilibrium phase diagram. First, the high-Zn incorporation is difficult to achieve because of the aforementioned high stability of ZnSe. On the other hand, the incorporation can be tuned to decrease the concentration of Sn_{Zn}. The low Sn incorporation, together with the low Zn incorporation, will, however, result in the formation of the highly conductive secondary phases of CuSe and Cu_2Se (see Fig. 3a), which can electrically short the device.[55] Thus, the low Sn incorporation should actually be avoided. We also find the hole concentrations are high under all conditions due to the high concentrations of Cu_{Zn}, which is also the consequence of the poor Zn incorporation. Therefore, it is difficult to decrease the concentrations of Sn_{Zn} in thermal equilibrium.

Fig. 6a shows the equilibrium concentrations of native defects under Se-poor and Se-rich conditions (see Fig. 3a). Under Se-poor conditions, we find high concentration of V_{Se}–Cu_{Zn}, which is an

efficient recombination center. While their concentrations can be significantly decreased through Se incorporation, the concentration of Sn_{Zn} can not be decreased below 10^{14} cm^{-3}, which limits the maximum performance of CZTSe solar cells.

Finally, we stress that the capture cross section and defect concentrations of the dominant recombination center in CZTSe (Sn_{Zn}) are in good agreement with experiments.[40,56] Our previous admittance spectroscopy[40] revealed a deep defect level located at 0.5 eV. Based on the thermal emission prefactors of up to 5×10^{12} cm s^{-1} at room temperature, we estimate the capture cross section as 1×10^{-13} cm^2 which agrees well with our calculation of 9×10^{-14} cm^2 (see Table S3, ESI†). We also find the longest minority-carrier lifetime achievable is less than 5.5 ns in CZTSe which closely agrees with the previous assessment of the real minority-carrier lifetime of below 1 ns based on time-resolved photoluminescence.[56,57]

Trap-limited conversion efficiency. We calculate the current–voltage characteristic (eqn (16)) of a CZTSe solar cell containing
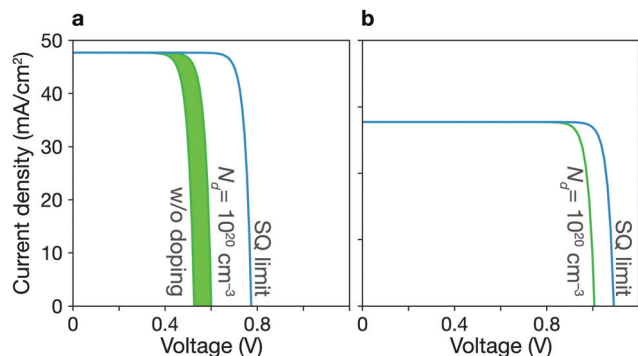
1486 | *Energy Environ. Sci.*, 2020, **13**, 1481–1491

This journal is © The Royal Society of Chemistry 2020

Fig. 7 Current–voltage simulation. J–V curves for CZTSe (a) and AZTSe (b) solar cells based on the properties of the bulk absorber materials and not including interfacial processes. Green lines represent the TLCs with various doping concentrations up to 10^{20} cm^{-3}. The SQ limit is shown in the blue curve.

the equilibrium concentrations of native point defects under the Se-rich condition (see Fig. 7a). We used the a film thickness of 2 μm. The overall power-conversion efficiency is 20.3%, which is below two thirds of the SQ limit of 31.6% (see Fig. 2 and Table 1).

Sulfide kesterite. Cu$_2$ZnSnS$_4$ (CZTS) also suffers from non-radiative recombination due to the redox activity of Sn and the narrow phase space limited by the high stability of ZnS. Similar to Sn$_{Zn}$ in CZTSe, we find the large structural relaxation for Sn$_{Zn}$ that causes fast carrier capture. Moreover, although the defect complex Sn$_{Zn}$–Cu$_{Zn}$ is a shallow donor in CZTSe, in CZTS having the larger band gap of 1.5 eV, Sn$_{Zn}$–Cu$_{Zn}$ produces the deep donor level at $E_T = 0.90$ eV as shown in Fig. 4a and b. Thus, the recombination pathways in CZTS are not only through the isolated Sn$_{Zn}$ but also the Sn$_{Zn}$ bound to the acceptor Cu$_{Zn}$, which agrees well with a previous theoretical study.[51] We find

that the similar behavior for Ge$_{Zn}$ in Cu$_2$ZnGeSe$_4$ which will be discussed in detail in the following section. We calculate a nonradiative V_{OC} loss of 0.39 V, corresponding to an achievable V_{OC} of 0.84 V and a maximum TLC of 20.9% for CZTS, which is similar to that of CZTSe.

B. Cu$_2$ZnGeSe$_4$

As the redox activity of Sn is one culprit that reduces the voltage and efficiency of CZTSe and CZTS devices, we can suppress the nonradiative recombination by substituting Sn with other cations such as Si with a more stable 4+ oxidation state. However, the SQ limit of Cu$_2$ZnSiSe$_4$ is below 16% because of its large band gap of 2.33 eV.[58] On the other hand, Cu$_2$ZnGeSe$_4$ (CZGSe) has an optimal band gap of 1.36 eV with an SQ limit of 33.6%. However, we find that the similar redox activity of Ge in CZGSe causes significant nonradiative recombination and limits the V_{OC}.

Ge also exhibits an inert-pair effect with large ionisation energy for the 4s orbital. Thus, Ge-related defects (Ge$_{Zn}$, Ge$_{Zn}$–Cu$_{Zn}$, V$_{Se}$ and V$_{Se}$–Cu$_{Zn}$) introduce deep donor levels in the band gap. Ge$_{Zn}$ exhibits the similar potential energy surfaces to those of Sn$_{Zn}$ in CZTSe (Fig. 5b). However, Ge$_{Zn}$ has a deeper donor level than that of Sn$_{Zn}$ due to the larger band gap of CZGSe (see Table S2, ESI†). As shown in Fig. 5, because the electron-capture processes due to Sn$_{Zn}$ and Ge$_{Zn}$ are in the so-called "Marcus inverted region",[59] the deeper donor level of Ge$_{Zn}$ results in a higher energy barrier for electron-capture (0.62 eV). We find a several orders of magnitude smaller electron-capture coefficient for Ge$_{Zn}$ (2+/1+) as compared to that of Sn$_{Zn}$ (2+/1+), implying that the recombination due to the isolated Ge$_{Zn}$ is unlikely to happen (see Table S3, ESI†).

However, the nonradiative recombination rate in CZGSe is still high due to defect complexation. The abundant acceptor Cu$_{Zn}$ tends to form a defect complex with donors such as Ge$_{Zn}$. The Coulomb attraction between the ionized donor and acceptor further promote the formation of the complex. Moreover, the donor–acceptor complex makes the defect level shallower ($E_T = 0.87$ eV).[50] We find that the electron-capture barrier is 71 meV for Ge$_{Zn}$–Cu$_{Zn}$ (1+/0), which is the dominant recombination pathway in CZGSe. Although, we considered only the Ge$_{Zn}$ and Cu$_{Zn}$ pair bound at the closest site, in reality, there are a variety of complexes with a wide range of distances between Sn$_{Zn}$ and Cu$_{Zn}$. Such a spectrum of complexes are partially responsible for the broad defect levels in kesterites measured in photocapacitance spectroscopies.[47,48]

By taking into account the formation of defect complexes, we find significant nonradiative loss in CZGSe. The maximum efficiency is predicted to be 24.1% with large non-radiative open-circuit voltage loss of 0.29 V (see Fig. 2 and Table 1).

C. Hydrogen and alkali-metal doping, and Ag$_2$ZnSnSe$_4$

As an additional lever to tune the defect profiles, we consider extrinsic doping. The formation energy, and hence concentration, of a defect depends on the chemical potential of an electron (Fermi level). In CZTSe, CZTS, and CZGSe, the intrinsic Fermi levels are pinned ~0.2 eV above the valence band

Table 1 Device performance parameters of selected Cu and Ag kesterite solar cells and predicted by Shockley–Queisser limit and trap-limited conversion efficiency and found experimentally (Exp.)

	E_{gap} (eV)	η (%)	J_{SC} (mA cm^{-2})	V_{OC} (V)	FF (%)	Ref.
CZTS	1.50	32.1	28.9	1.23	90.0	SQ limit
CZTSe	1.00	31.6	47.7	0.77	85.7	SQ limit
CZGSe	1.36	33.3	34.3	1.10	89.1	SQ limit
AZTSe	1.35	33.7	34.7	1.09	89.0	SQ limit
CZTS	1.50	20.9	28.9	0.84	86.4	TLC
CZTSe	1.00	20.3	47.7	0.53	81.0	TLC
CZGSe	1.36	24.1	34.3	0.81	86.2	TLC
CZTS:H	1.50	23.1	28.9	0.91	87.4	TLC
CZTSe:H	1.00	23.7	47.7	0.60	82.7	TLC
CZGSe:H	1.36	27.9	34.3	0.93	87.5	TLC
AZTSe:H	1.35	30.8	34.7	1.01	88.1	TLC
CZTS	1.50	11.0	21.7	0.73	69.27	Exp.[25]
CZTSe	1.00	11.6	40.6	0.42	67.3	Exp.[70]
CZTSSe	1.13	12.6	35.4	0.54	65.9	Exp.[6]
CZTGSe	1.11	12.3	32.3	0.53	72.7	Exp.[22]
CZGSe	1.36	7.6	22.8	0.56	60	Exp.[26]
AZTSe	1.35	5.2	21.0	0.50	48.7	Exp.[23]
ACZCTS	1.40	10.1	23.4	0.65	66.2	Exp.[24]

This journal is © The Royal Society of Chemistry 2020

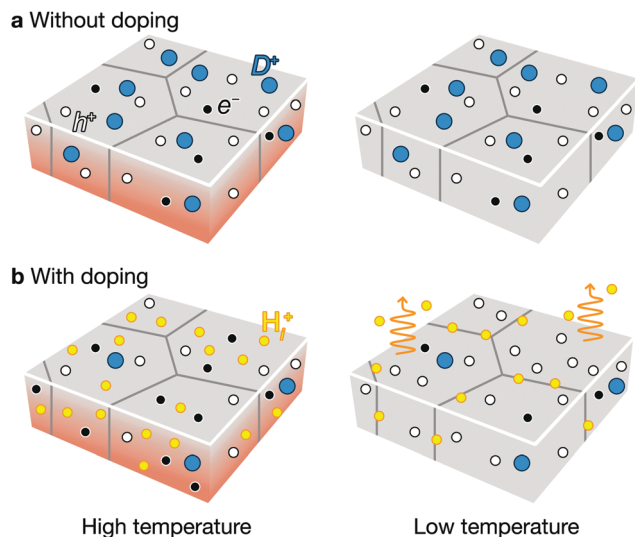*Energy Environ. Sci.*, 2020, **13**, 1481–1491 | **1487**

Fig. 8 The effect of hydrogen/alkali-metal doping on kesterites. Schematics for the formation of defects without doping (a) and with doping (b). During thermal annealing, the native defects are formed at high temperature (left panel), whose populations remain the same when the sample is cooled down to low temperature (right panel). A high concentration of hole (white circle) promote the formation of donors (blue circle). Dopants are marked as yellow circles. For the clarity, the acceptors are not drawn.

(Fig. 4a–c), promoting the formation of deep donors. As illustrated in Fig. 8a, such high concentrations of donors arise at high (growth) temperature and remain after cooling because they are mostly immobile vacancies and antisites. While n-type doping can increase the Fermi level, this type of doping will not increase the V_{OC} (efficiency) for a material with limited minority carrier lifetime, because n-type doping will decrease the p-type conductivity.

Instead, we predict that hydrogen and alkali-metal doping is helpful to increase the efficiency. At high temperature during the thin-film growth or thermal annealing, the incorporation of the hydrogen or alkali metals at the interstitial sites will increase the Fermi level as they act as donors in p-type semiconductors.[60] The high Fermi level decreases the hole concentration and the formation of donor type defects as well (see Fig. 8c). Since hydrogen and alkali-metals are mobile, they tend to diffuse easily and segregate to the grain boundary or outgas, when the thin-film cools down to the room temperature (see Fig. 8d). The final thin-film will exhibit an increased hole concentration and longer carrier lifetime, consistent with the experiments.[61] This is indeed the mechanism behind the success of hydrogen-codoping in nitride semiconductors.[62,63]

We calculate the concentrations of defects in CZTSe with a n-type doping concentration of 10^{20} cm^{-3} at $T = T_{an}$. Once the dopants are removed, the hole concentration increases by an order of magnitude at $T = T_{op}$, and the concentration of Sn$_{Zn}$ is significantly lowered (see Fig. 6a). Thus, the maximum efficiency increases up to 23.7% (Fig. 2 and 7a). This requires a high level of doping to gain a noticeable improvement due to the high concentration of native donors and acceptors, and the self-compensation mechanism *via* them. Alkali-metal elements may be less effective dopants due to their low solubility.[61]

On the other hand, the previous calculations[60] have shown that the formation energies of H$_i$ in kesterites are low at p-type Fermi-level, suggesting high solubility of H in kesterites. We also noted that Son *et al.* formed a S–Se grading in the current champion device[6] using H$_2$S gas, which may introduce the H-doping unintentionally and be responsible for the high efficiency.

The low formation energies and the high concentrations of Cu$_{Zn}$ and Zn$_{Cu}$ originate from the similar ionic radii of Cu^{1+} and Zn^{2+}. We may decrease their concentrations by exploiting Ag substituting Cu or Cd substituting Zn.[64] Ag substitution for Cu gives Ag$_2$ZnSnSe$_4$ (AZTSe), which also has a narrow phase diagram as shown in Fig. 3b. However, we find several orders of magnitude lower concentrations of the dominant acceptor and donor, Ag$_{Zn}$ and Zn$_{Ag}$ (see Fig. 6b). AZTSe is an intrinsic semiconductor under Se-rich conditions, while n-type Fermi level was found under Se-poor conditions.

For a set of atomic chemical potentials determined under Se-rich conditions, the calculated self-consistent Fermi-level is 0.55 eV above the valence band. Due to the low hole concentration in AZTSe, eqn (6) is not valid, and the hole-capture process becomes the bottleneck in the recombination process owing to the high hole-capture barrier of 0.20 eV as compared to the electron-capture barrier of 0.11 eV. However, due to the high Fermi level in AZTSe or even n-type conductivity, Ag-based solar cells based on the commonly used thin-film architecture for Cu-based kesterites (Mo/kesterite/CdS/ZnO/ITO), have been found to exhibit limited device performance.[23,65,66] Notwithstanding these practical challenges, we predict that Ag-based kesterites should show much lower non-radiative recombination and thus possess a significantly larger efficiency potential than the previously discussed Cu- or Ge-based kesterites. Indeed, increased photoluminescence quantum yields (PLQY) have been recently observed for Ag-substituted kesterites.[67]

An extrinsic n-type doping level of 10^{20} cm^{-3} during growth can lower the room temperature Fermi-level to 0.18 eV. As shown in Fig. 6b, this causes the concentration of Sn$_{Zn}$ to decrease below 10^{14} cm^{-3}, enhancing the maximum efficiency up to 30.8% (see Fig. 2 and 7), implying that co-doped AZTSe is a promising material as a p-type absorber if the synthesis and processing be appropriately controlled.

D. Calculation of optoelectronic parameters

The achievable solar cell parameters estimated for four types of kesterite materials using our first-principles approach are summarized in Table 1, and compared with the (defect-free) Shockley–Queisser limit, as well as current champion devices.

The Ge- and Ag-based materials so far significantly underperform, and that big leaps in efficiency appear possible by the proposed co-doping strategy. Device performance can be limited by a number of non-idealities such as non-optimised functional layers, wrong band line-ups, as well as interface recombination. It is therefore helpful to consider the main (absorber layer) optoelectronic parameters that are experimentally accessible even without building devices. Among the most relevant to judge potential device performance are carrier lifetime, net doping density, and external PLQY, which indicates

1488 | *Energy Environ. Sci.*, 2020, **13**, 1481–1491

This journal is © The Royal Society of Chemistry 2020

Table 2 Optoelectronic parameters derived from first principles of selected Cu and Ag kesterites. ΔV_{OC}^{nonrad} is the V_{OC} loss due to the nonradiative recombination, p_0 is the intrinsic hole concentration, τ_{SRH} is the carrier lifetime and PLQY is the external photoluminescence quantum yield at 1 sun equivalent conditions

	E_{gap} (eV)	ΔV_{OC}^{nonrad} (V)	p_0 (cm^{-3})	τ_{SRH} (ns)	PLQY (%)
CZTS	1.50	0.39	3.3×10^{15}	0.13	3.1×10^{-5}
CZTSe	1.00	0.24	1.7×10^{15}	3.4	9.8×10^{-3}
CZGSe	1.36	0.29	9.0×10^{15}	0.21	1.4×10^{-3}
AZTSe	1.35		1.0×10^{10}		
CZTS:H	1.50	0.32	3.8×10^{16}	0.21	4.5×10^{-4}
CZTSe:H	1.00	0.17	1.8×10^{16}	5.5	1.5×10^{-1}
CZGSe:H	1.36	0.17	4.8×10^{17}	0.38	1.5×10^{-1}
AZTSe:H	1.35	0.08	1.7×10^{16}	1130	4.6

the ratio of radiative recombination over the total recombination, typically dominated by non-radiative processes. The PLQY can be estimated from non-radiative voltage loss using $\Delta V_{OC}^{nonrad} = k_B T \ln(\text{PLQY})$.[68]

A summary of these parameters, calculated from first-principles, are listed in Table 2, indicating small PLQY and lifetimes for CZTS and large PLQY and long lifetimes for co-doped AZTSe. The small predicted PLQY for CZTS is in agreement with observations that the luminescence yield of this material is consistently below the detection limit (*ca.* 1×10^{-4}%). Also, the PLQY value of 1×10^{-2}% is consistent with recent reports of 1.5×10^{-3}% measured on a CZTSe single crystal[57] and of 3×10^{-3}% on 11.6% efficient Li-doped CZTSSe solar cells.[69]

In these solar cells the lifetime did not change significantly with Li-doping, while the PLQY and net doping density increased, again inline with our predictions. With regards to the calculated minority carrier lifetimes, we point out that the small estimated lifetimes for CZTS and CZTSe are in good agreement with recent findings indicating that reported carrier lifetimes for kesterites are often overestimated and that (typical) real lifetimes are in fact below 1 ns.[56]

III. Conclusions

We have combined the physics of solar cells with modern first-principles defect theory to assess the efficiency limit of solar cells. We have included the thermal equilibrium concentrations of native defects of the absorber material, which reduces carrier lifetime, and have proposed a first-principles method to calculate the maximum efficiency limited by recombination centers. Sn-Based kesterites suffer from severe nonradiative recombination due to native point defects. The fast nonradiative recombination can be mitigated by extrinsic doping and Ag-alloying, reducing the concentration of recombination centres, thereby increasing the performance threshold to 29%.

Although, our approach advances first-principles approaches for solar cells, its limitations should be noted. We are pushing defect theory to its limits of applicability and note that inaccuracies, *e.g.* through finite-sized corrections or choice of exchange–correlation functional, will become magnified in the predictions of defect concentrations and capture cross-sections. The method

inherits some of the limitations of the SQ approach.[71] It is based on bulk properties and therefore does not take into account surface or interface recombination. Parasitic absorption effects in the buffer or window layers are also ignored.

In the case of kesterite solar cells, although it is widely accepted that a short carrier life is the main performance bottleneck,[9,56] high series resistance can further reduce efficiency.[9] Thin-films are often inhomogeneous with lateral variations in stoichiometry. Therefore, fluctuations of the band gap and the electrostatic potential can reduce the open-circuit voltage beyond our predictions.[72]

The TLC metric should be considered as an upper bound, based on the bulk properties of the absorber, that can be achieved when losses through other degradation pathways are minimal. In commercial photovoltaic solar cells, J_{SC} and FF approach the SQ limit. The main efficiency-limiting factor is V_{OC},[71,73] which we tackle. Therefore, our method can provide a new direction for searching for promising photovoltaic materials by providing a realistic upper limit on expected performance. It can be used as part of screening procedures to select viable candidates. Finally, we emphasise that to assess the genuine potential of real materials for photovoltaics, one should consider not only the thermodynamics of light and electrons, but also the thermodynamics of crystals.

IV. Data availability

The data that support the findings of this study are available in Zenodo repository with the identifier DOI: 10.5281/zenodo.3585618. The code used in this study is available in Zenodo repository with the identifier DOI: 10.5281/zenodo.3700743. We make use of the open-source packages https://github.com/WMD-group/CarrierCapture.jl (capture cross-sections), https://github.com/jbuckeridge/sc-fermi (equilibrium concentrations) and https://github.com/jbuckeridge/cplap (chemical stability fields).

Conflicts of interest

There are no conflicts to declare.

Acknowledgements

References

1 P. T. Landsberg and G. Tonge, *J. Appl. Phys.*, 1980, **51**, R1–R20.

2 A. Mart and G. L. Araújo, *Sol. Energy Mater. Sol. Cells*, 1996, **43**, 203–222.

3 W. Shockley and H. J. Queisser, *J. Appl. Phys.*, 1961, **32**, 510–519.

4 L. Yu and A. Zunger, *Phys. Rev. Lett.*, 2012, **108**, 068701.

5 M. A. Green, E. D. Dunlop, D. H. Levi, J. Hohl-Ebinger, M. Yoshita and A. W. Y. Ho-Baillie, *Prog. Photovoltaics*, 2019, **27**, 565–575.

6 D.-H. Son, S.-H. Kim, S.-Y. Kim, Y.-I. Kim, J.-H. Sim, S.-N. Park, D.-H. Jeon, D.-K. Hwang, S.-J. Sung, J.-K. Kang, K.-J. Yang and D.-H. Kim, *J. Mater. Chem. A*, 2019, **132**, 17384.

7 W. Wang, M. T. Winkler, O. Gunawan, T. Gokmen, T. K. Todorov, Y. Zhu and D. B. Mitzi, *Adv. Energy Mater.*, 2013, **4**, 1301465.

8 S. K. Wallace, D. B. Mitzi and A. Walsh, *ACS Energy Lett.*, 2017, **2**, 776–779.

9 L. Grenet, M. A. A. Suzon, F. Emieux and F. Roux, *ACS Appl. Energy Mater.*, 2018, **1**, 2103.

10 S. Siebentritt, *Thin Solid Films*, 2013, **535**, 1–4.

11 S. Bourdais, C. Choné, B. Delatouche, A. Jacob, G. Larramona, C. Moisan, A. Lafond, F. Donatini, G. Rey and S. Siebentritt, *et al.*, *Adv. Energy Mater.*, 2016, **6**, 1502276.

12 S. Schorr, G. Gurieva, M. Guc, M. Dimitrievska, A. Pérez-Rodrguez, V. Izquierdo-Roca, C. S. Schnohr, J. Kim, W. Jo and J. M. Merino, *J. Phys.: Energy*, 2019, **2**, 12002, DOI: 10.1088/2515-7655/ab4a25.

13 W. Shockley and W. T. Read, *Phys. Rev.*, 1952, **87**, 835.

14 R. N. Hall, *Phys. Rev.*, 1952, **87**, 387.

15 C. H. Henry and D. V. Lang, *Phys. Rev. B: Condens. Matter Mater. Phys.*, 1977, **15**, 989.

16 L. Shi and L.-W. Wang, *Phys. Rev. Lett.*, 2012, **109**, 245501.

17 A. Alkauskas, Q. Yan and C. G. Van de Walle, *Phys. Rev. B: Condens. Matter Mater. Phys.*, 2014, **90**, 075202.

18 S. Kim, S. N. Hood and A. Walsh, *Phys. Rev. B*, 2019, **100**, 041202(R).

19 U. Rau, B. Blank, T. C. M. Müller and T. Kirchartz, *Phys. Rev. Appl.*, 2017, **7**, 044016.

20 J.-S. Park, S. Kim, Z. Xie and A. Walsh, *Nat. Rev. Mater.*, 2018, **3**, 194–210.

21 J. Nelson, *The Physics of Solar Cells*, Imperial College Press, London, UK, 2003.

22 S. Kim, K. M. Kim, H. Tampo, H. Shibata and S. Niki, *Appl. Phys. Express*, 2016, **9**, 102301.

23 T. Gershon, K. Sardashti, O. Gunawan, R. Mankad, S. Singh, Y. S. Lee, J. A. Ott, A. Kummel and R. Haight, *Adv. Energy Mater.*, 2016, **6**, 1601182.

24 S. H. Hadke, S. Levcenko, S. Lie, C. J. Hages, J. A. Marquez, T. Unold and L. H. Wong, *Adv. Energy Mater.*, 2018, **18**, 1802540.

25 C. Yan, J. Huang, K. Sun, S. Johnston, Y. Zhang, H. Sun, A. Pu, M. He, F. Liu, K. Eder, L. Yang, J. M. Cairney, N. J. Ekins-Daukes, Z. Hameiri, J. A. Stride, S. Chen, M. A. Green and X. Hao, *Nat. Energy*, 2018, **3**, 764.

26 L. Choubrac, G. Brammertz, N. Barreau, L. Arzel, S. Harel, M. Meuris and B. Vermang, *Phys. Status Solidi A*, 2018, **215**, 1800043.

27 J. Buckeridge, D. O. Scanlon, A. Walsh and C. R. A. Catlow, *Comput. Phys. Commun.*, 2014, **185**, 330.

28 C. Freysoldt, B. Grabowski, T. Hickel, J. Neugebauer, G. Kresse, A. Janotti and C. G. Van de Walle, *Rev. Mod. Phys.*, 2014, **86**, 253.

29 C. Freysoldt, J. Neugebauer and C. G. Van de Walle, *Phys. Rev. Lett.*, 2009, **102**, 016402.

30 Y. Kumagai and F. Oba, *Phys. Rev. B: Condens. Matter Mater. Phys.*, 2014, **89**, 195205.

31 J. Buckeridge, *Comput. Phys. Commun.*, 2019, **244**, 329–342.

32 A. Walsh, A. A. Sokol and C. R. A. Catlow, *Phys. Rev. B: Condens. Matter Mater. Phys.*, 2011, **83**, 224105.

33 R. Pässler, *Phys. Status Solidi B*, 1976, **78**, 625–635.

34 P. T. Landsberg, *Recombination in Semiconductors*, Cambridge University Press, Cambridge, UK, 2009.

35 A. Zakutayev, C. M. Caskey, A. N. Fioretti, D. S. Ginley, J. Vidal, V. Stevanovic, E. Tea and S. Lany, *J. Phys. Chem. Lett.*, 2014, **5**, 1117.

36 A. Walsh and A. Zunger, *Nat. Mater.*, 2017, **50**, 797.

37 S. Kim, J.-S. Park and A. Walsh, *ACS Energy Lett.*, 2018, **3**, 496–500.

38 O. Gunawan, T. Gokmen, C. W. Warren, J. D. Cohen, T. K. Todorov, D. A. R. Barkhouse, S. Bag, J. Tang, B. Shin and D. B. Mitzi, *Appl. Phys. Lett.*, 2012, **100**, 253905.

39 D. B. Khadka, S. Kim and J. Kim, *J. Phys. Chem. C*, 2015, **119**, 12226.

40 S. Levcenko, J. Just, A. Redinger, G. Larramona, S. Bourdais, G. Dennler, A. Jacob and T. Unold, *Phys. Rev. Appl.*, 2016, **5**, 024004.

41 M. J. Koeper, C. J. Hages, J. V. Li, D. Levi and R. Agrawal, *Appl. Phys. Lett.*, 2017, **111**, 142105.

42 K.-J. Yang, S. Kim, J.-H. Sim, D.-H. Son, D.-H. Kim, J. Kim, W. Jo, H. Yoo, J. Kim and J.-K. Kang, *Nano Energy*, 2018, **52**, 38.

43 K.-J. Yang, S. Kim, S.-Y. Kim, K. Ahn, D.-H. Son, S.-H. Kim, S.-J. Lee, Y.-I. Kim, S.-N. Park, S.-J. Sung, D.-H. Kim, T. Enkhbat, J. Kim, C.-W. Jeon and J.-K. Kang, *Nat. Commun.*, 2019, **10**, 2959.

44 J. V. Li, D. Kuciauskas, M. R. Young and I. L. Repins, *Appl. Phys. Lett.*, 2013, **102**, 163905.

45 S. Das, S. K. Chaudhuri, R. N. Bhattacharya and K. C. Mandal, *Appl. Phys. Lett.*, 2014, **104**, 192106.

46 V. Kheraj, E. A. Lund, A. E. Caruso, K. Al-Ajmi, D. Pruzan, C. Miskin, R. Agrawal, C. Beall, I. Repins and M. A. Scarpulla, *IEEE 43rd Photovoltaic Specialists Conference*, 2016, p. 2195.

47 D. W. Miller, C. W. Warren, O. Gunawan, T. Gokmen, D. B. Mitzi and J. D. Cohen, *Appl. Phys. Lett.*, 2012, **101**, 142106.

48 M. M. Islam, M. A. Halim, T. Sakurai, N. Sakai, T. Kato, H. Sugimoto, H. Tampo, H. Shibata, S. Niki and K. Akimoto, *Appl. Phys. Lett.*, 2015, **106**, 243905.

49 D. Han, Y. Y. Sun, J. Bang, Y. Y. Zhang, H.-B. Sun, X.-B. Li and S. B. Zhang, *Phys. Rev. B: Condens. Matter Mater. Phys.*, 2013, **87**, 155206.

50 S. Kim, J.-S. Park, S. N. Hood and A. Walsh, *J. Mater. Chem. A*, 2019, **7**, 2686.

51 J. Li, Z.-K. Yuan, S. Chen, X.-G. Gong and S.-H. Wei, *Chem. Mater.*, 2019, **31**, 826.

1490 | *Energy Environ. Sci.*, 2020, **13**, 1481–1491

This journal is © The Royal Society of Chemistry 2020

52 A. M. Stoneham, *Theory of Defects in Solids*, Oxford University Press, Cambridge, UK, 1975.

53 D. Macdonald and L. J. Geerligs, *Appl. Phys. Lett.*, 2004, **85**, 4061–4063.

54 A. R. Peaker, V. P. Markevich, B. Hamilton, G. Parada, A. Dudas, A. Pap, E. Don, B. Lim, J. Schmidt, L. Yu, Y. Yoon and G. Rozgonyi, *Phys. Status Solidi A*, 2012, **209**, 1884–1893.

55 M. Dimitrievska, A. Fairbrother, E. Saucedo, A. Perez-Rodriguez and V. Izquierdo-Roca, *Sol. Energy Mater. Sol. Cells*, 2016, **149**, 304–309.

56 C. J. Hages, A. Redinger, S. Levcenko, H. Hempel, M. J. Koeper, R. Agrawal, D. Greiner, C. A. Kaufmann and T. Unold, *Adv. Energy Mater.*, 2017, **7**, 1700167.

57 S. Li, M. A. Lloyd, H. Hempel, C. J. Hages, J. A. Márquez, T. Unold, R. Eichberger, B. E. McCandless and J. B. Baxter, *Phys. Rev. Appl.*, 2019, **11**, 034005.

58 Q. Shu, J.-H. Yang, S. Chen, B. Huang, H. Xiang, X.-G. Gong and S.-H. Wei, *Phys. Rev. B: Condens. Matter Mater. Phys.*, 2013, **87**, 115208.

59 R. A. Marcus and N. Sutin, *Biochim. Biophys. Acta*, 1985, **811**, 265–322.

60 J. B. Varley, V. Lordi, T. Ogitsu, A. Deangelis, K. Horsley and N. Gaillard, *J. Appl. Phys.*, 2018, **123**, 161408.

61 S. G. Haass, C. Andres, R. Figi, C. Schreiner, M. Bürki, Y. E. Romanyuk and A. N. Tiwari, *Adv. Energy Mater.*, 2017, **6**, 1701760.

62 S. Nakamura, *Rev. Mod. Phys.*, 2015, **87**, 1139–1151.

63 A. N. Fioretti, A. Stokes, M. R. Young, B. Gorman, E. S. Toberer, A. C. Tamboli and A. Zakutayev, *Adv. Electron. Mater.*, 2017, **3**, 1600544.

64 G. S. Gautam, T. P. Senftle and E. A. Carter, *Chem. Mater.*, 2018, **30**, 4543–4555.

65 T. Gershon, O. Gunawan, T. Gokmen, K. W. Brew, S. Singh, M. Hopstaken, J. R. Poindexter, E. S. Barnard, T. Buonassisi and R. Haight, *J. Appl. Phys.*, 2017, **121**, 174501.

66 Y. Jiang, B. Yao, J. Jia, Z. Ding, R. Deng, D. Liu, Y. Sui, H. Wang and Y. Li, *J. Appl. Phys.*, 2019, **125**, 025703.

67 G. Gurieva, J. A. Márquez, A. Franz, C. J. Hges, S. Levcenko, T. Unold and S. Schorr, under review.

68 R. T. Ross, *J. Chem. Phys.*, 1967, **46**, 4590–4593.

69 A. Cabas-Vidani, S. G. Haass, C. Andres, R. Caballero, R. Figi, C. Schreiner, J. A. Márquez, C. Hages, T. Unold and D. Bleiner, *et al.*, *Adv. Energy Mater.*, 2018, **8**, 1801191.

70 Y. S. Lee, T. Gershon, O. Gunawan, T. K. Todorov, T. Gokmen, Y. Virgus and S. Guha, *Adv. Energy Mater.*, 2014, **5**, 1401372.

71 J.-F. Guillemoles, T. Kirchartz, D. Cahen and U. Rau, *Nat. Photonics*, 2019, **13**, 501.

72 J. Mattheis, J. H. Werner and U. Rau, *Phys. Rev. B: Condens. Matter Mater. Phys.*, 2008, **77**, 085203.

73 P. K. Nayak, S. Mahesh, H. J. Snaith and D. Cahen, *Nat. Rev. Mater.*, 2019, **4**, 269.

This journal is © The Royal Society of Chemistry 2020

Energy Environ. Sci., 2020, **13**, 1481–1491 | **1491**